Geophysical Research Letters

RESEARCH LETTER
10.1029/2019GL084843

MMS Observations of Plasma Heating Associated With FTE Growth

M. Akhavan-Tafti[1], J. A. Slavin[1], W. J. Sun[1], G. Le[2], and D. J. Gershman[2]

[1]Climate and Space Sciences and Engineering, University of Michigan, Ann Arbor, MI, USA, [2]NASA Goddard Space Flight Center, Greenbelt, MD, USA

Key Points:
- The relative roles of parallel electric fields, betatron, and Fermi processes in plasma heating inside 55 subsolar FTEs are determined
- Parallel electric fields dominate plasma energization at FTEs' leading edge. Betatron and Fermi processes overtake at FTEs' trailing edge
- MMS observations reveal strong plasma acceleration inside FTEs that is inversely proportional to the square root of FTE diameter

Supporting Information:
- Supporting Information S1
- Data Set S1

Correspondence to:
M. Akhavan-Tafti,
akhavant@umich.edu

Citation:
Akhavan-Tafti, M., Slavin, J. A., Sun, W. J., Le, G., & Gershman, D. J. (2019). MMS observations of plasma heating associated with FTE growth. *Geophysical Research Letters*, *46*, 12,654–12,664. https://doi.org/10.1029/2019GL084843

Received 2 AUG 2019
Accepted 6 NOV 2019
Accepted article online 11 NOV 2019
Published online 21 NOV 2019

Abstract Upon formation, flux transfer events (FTEs) in the subsolar magnetosheath have been observed to grow in diameter, λ, while convecting along the magnetopause. Plasma pressure has also been found to decrease sub-adiabatically with increasing λ, indicating the presence of internal plasma acceleration and heating processes. Here, the Magnetospheric Multiscale (MMS) fields and plasma measurements are used to determine the relative roles of parallel electric fields, betatron, and Fermi processes in plasma heating inside an ensemble of 55 subsolar FTEs. Plasma heating is shown asymmetric inside FTEs. Parallel electric fields dominate (>75%) ion and electron heating at the leading edge of FTEs. At the trailing edge, betatron and Fermi processes overtake (>50%), resulting in ion cooling and electron heating, respectively. The observed strong net heatings inside FTEs are proportional to $\lambda^{-1/2}$. It is concluded that reconnection-driven heating continues inside FTEs far from the subsolar electron and ion diffusion regions.

Plain Language Summary Energetic charged particles are observed in many space and astrophysical environments, including our solar system. However, the acceleration and heating mechanisms responsible for generating these energetic charged particles remain to be discovered. Simulations and in situ observations have shown that magnetic reconnection, a process through which magnetic field lines "reconnect" and release magnetic energy, plays a major role in generating energetic charged particles. The primary sites for magnetic energy transfer to charged particle acceleration and heating are the twin exhaust regions that emanate from the reconnection X-line. However, the amount of kinetic energy gained by charged particles in the exhaust regions represents only a small fraction of the total energy released by magnetic reconnection. Here, the Magnetospheric Multiscale (MMS) multipoint fields and plasma measurements are used to determine the contributions of acceleration mechanisms operating inside flux transfer events (FTEs), which are formed in the reconnection exhaust regions. We observe that acceleration mechanisms contribute to the charged particles' energy gain inside FTEs. We further reveal that while acceleration mechanisms are most significant inside smaller FTEs, they continue to accelerate charged particles inside larger FTEs. We conclude that magnetic reconnection-driven charged particle acceleration is long-lasting and can take place far from the exhaust regions.

1. Introduction

Satellite observations have long reported the presence of energetic particles, emanating from the solar corona, in the interplanetary medium and in planetary magnetospheres (e.g., Baker & Stone, 1977; Dewey et al., 2017; Huang et al., 2012; Krimigis & Sarris, 1979; Meng, 1971; Meng & Anderson, 1971; Murayama & Simpson, 1968; Retinò et al., 2008; Retzler & Simpson, 1969; Sarris et al., 1976). The key outstanding questions regard the underlying physical mechanisms producing such energetic particles and their transport. The proposed mechanisms include fast and slow shocks, electromagnetic waves, and magnetic reconnection (e.g., Aschwanden, 2002; Benz, 2017; Drake et al., 2006; Guo et al., 2015; Krucker et al., 2008; Miller et al., 1997).

Particle-in-cell simulations and in situ observations have attributed magnetic reconnection-driven plasma acceleration and heating to three major mechanisms (e.g., Chen et al., 2008; Dahlin et al., 2014, 2015, 2016, 2017; Kagan et al., 2017; Büchner et al., 2018). In the first mechanism, plasma acceleration and heating occur inside or near the diffusion region, where collisionless plasma processes facilitate the changes in magnetic connection through the generation of dissipative electric fields (e.g., Bessho & Bhattacharjee, 2012;

Cerutti et al., 2012; Lyubarsky & Liverts, 2008; Oka et al., 2010; Uzdensky et al., 2011; Zenitani & Hoshino, 2001, 2007, 2008). Secondly, acceleration and heating occur in the downstream of the reconnection site, between an adjacent X-line and the edges of a flux rope, where the outflowing plasma first encounters sharp spatial magnetic field variations (i.e., strong magnetic field gradients) (e.g., Hoshino et al., 2001; Jaroschek et al., 2004; Pritchett, 2008; Zenitani & Hoshino, 2007). Thirdly, acceleration and heating occur inside flux ropes, where the newly reconnected magnetic flux piles up, and particles can become accelerated (Drake et al., 2006, 2010; Kowal et al., 2011).

Simulations suggest that plasmas are accelerated along reconnecting magnetic field lines due to parallel electric fields and curvature drift, that is, Fermi acceleration (Dahlin et al., 2014; Muñoz & Buechner, 2017). In the guiding center limit, where the first adiabatic invariant is conserved, plasma acceleration is described by (Drake et al., 2019; Northrop, 1963)

$$ {}^{dU}\!/_{dt} = \dot{U} = E_{\parallel} J_{\parallel} + {}^{p_{\perp}}\!/_{B} \left({}^{\partial B}\!/_{\partial t} + \mathbf{u}_E \cdot \nabla \mathbf{B} \right) + \left(p_{\parallel} + \rho u_{\parallel}^2 \right) \mathbf{u}_E \cdot \boldsymbol{\kappa}, $$

where U is the total kinetic energy, $p_{\parallel}$ and $p_{\perp}$are the parallel and perpendicular (with respect to the ambient magnetic field B) thermal pressures, respectively. $\boldsymbol{u}_E$ is the E × B drift velocity. ρ and $u_{\parallel}$ denote the mass density and the parallel bulk velocity, respectively, and the curvature $\boldsymbol{\kappa} = (\mathbf{B} \cdot \nabla)\,\mathbf{B}/B^2$. Term 1 ($\dot{U}_1$: parallel electric fields) the first term on the right-hand side, describes acceleration due to parallel electric fields and is independent of frame of reference. Conservation of the first adiabatic invariant, μ, is invoked in the second term, Term 2 ($\dot{U}_2$: betatron process). Here, the gradient B drift accelerates particles via betatron acceleration. The last term, Term 3 ($\dot{U}_3$: first-order Fermi process), describes curvature drift driven by relaxing magnetic field lines, which accelerate particles parallel to B through Fermi acceleration.

The simulations by Egedal et al. (2012) suggested that parallel electric fields can accelerate electrons over spatial scales larger than the previously thought electron diffusion regions. Later simulations by Dahlin et al. (2016) contradicted these results. Instead, the authors argued that Fermi acceleration dominates electron heating, especially in regimes of strong magnetic shear. These results were re-examined by Zhou et al. (2018) using three-dimensional particle-in-cell simulations. They concluded that parallel electric fields are the dominant electron acceleration mechanism. More notably, small-scale flux ropes were found to play an essential role in accelerating electrons, in agreement with the Cluster observations by Fu, Xu, et al. (2019).

Magnetospheric Multiscale (MMS) observations (Akhavan-Tafti et al., 2018) and simulations (Fermo et al., 2011; Hoilijoki et al., 2019; Raeder, 2006) indicate that flux transfer events (FTEs) form in the subsolar region and grow as they convect toward the flanks and high-latitude magnetopause. Internal plasma pressure is observed to decrease sub-adiabatically with increasing FTE diameter (Akhavan-Tafti et al., 2019) suggesting the presence of internal plasma acceleration and heating processes. Akhavan-Tafti et al. (2019) further showed the presence of residual net force inside FTEs, which can accelerate plasmas. Herein, we quantify the contributions of acceleration mechanisms in the guiding center approximation using MMS high temporal and spatial resolution fields and plasma measurements. First, a case study event is presented as a typical example of plasma moments and distributions across and in the environments surrounding two neighboring FTEs of different scale sizes. Next, the contributions of the parallel electric fields, betatron acceleration, and the first-order Fermi acceleration are determined directly from the MMS measurements inside and at the outer perimeters of 55 subsolar, quasi-force-free FTEs, identified by Akhavan-Tafti et al. (2018, 2019). It is concluded that magnetic reconnection plays a long-lasting role in accelerating plasmas at the magnetopause by generating FTE-type flux ropes, which then grow and further accelerate plasmas.

2. Methods

The multipoint analysis techniques are used to calculate spatial gradients, including magnetic gradient $\nabla \boldsymbol{b}$ and curvature $\boldsymbol{\kappa} = (\boldsymbol{B} \cdot \nabla)\,\boldsymbol{B}$ (Akhavan-Tafti et al., 2019; Zhao et al., 2016) at the barycenter of the four MMS spacecraft (Harvey, 1998). Plasma current density is determined from the fast plasma investigation (Pollock et al., 2016) plasma moments at the barycenter (Akhavan-Tafti et al., 2018). The four-spacecraft average plasma and electric field double probe (Ergun et al., 2016; Lindqvist et al., 2016; Torbert et al., 2016) electric field measurements are determined at the barycenter and interpolated to match the fluxgate magnetometer

(Russell et al., 2016) time resolution at 128 samples per second. The induced local magnetic fields is estimated from Faraday's law, $^{\partial \mathbf{B}}/_{\partial t} = -\nabla \times \mathbf{E}$, wherein the component along the E × B drift is calculated as $^{\partial B}/_{\partial t} = {}^{1}/_{|\boldsymbol{u}_E|}\left(\boldsymbol{u}_E \cdot {}^{\partial \mathbf{B}}/_{\partial t}\right)$, where $\boldsymbol{u}_E$ represents the E × B drift velocity. The four MMS spacecraft were maintained at a tetrahedron formation at an average separation of 10 km throughout the duration of the interval of interest (Burch et al., 2016).

FTEs are modeled as force-free flux ropes in order to determine their scale size, impact parameter (IP; defined as the relative distance from the FTE's central axis at the spacecraft closest approach, compare Figure 11 of Akhavan-Tafti et al., 2018), and geometry. Fifty-five FTE-type flux ropes are selected based on the following criteria: 1) small impact parameter (IP < 0.5), and 2) cylindrical symmetry (force-free model goodness of fit parameter, $\chi^2 < 0.1$; cf. Akhavan-Tafti et al., 2018, 2019).

3. Analysis and Results

3.1. Case Study

The magnetopause crossing of 17 November 2015 was first examined and reported by Zhou et al. (2017). The boundary crossing was marked by large ion jet reversals corresponding to a dissipative interaction of two neighboring FTEs. As shown in Figure1a, the magnetic field magnitude and vector components indicate the presence of two force-free FTEs (e.g., Akhavan-Tafti et al., 2019; Russell & Elphic, 1978), labeled as "FTE 1" and "FTE 2," centered at 02:20:48 UT and 02:21:24 UT. The FTEs are identified with their bipolar magnetic signatures coinciding with an enhancement in the axial and total magnetic fields. Plasma distribution along the field lines are used to identify FTE boundaries (e.g., Lv et al., 2016).

FTE 1 is 4,000 km in diameter, λ, with a modeled core field magnitude of 60 nT corresponding to a magnetic flux content 300 kWb (Akhavan-Tafti et al., 2018). FTE 2 is much smaller in scale, λ~2,000 km, has a weaker core magnetic field magnitude,|B|= 45 nT, and smaller flux content of 40 kWb. Using the timing analysis, it is estimated that FTE 1 and FTE 2 convect at speeds 100 and 180 km/s, respectively. Electrons and ions are found to remain frozen-in throughout the crossings.

The parallel $T_{i\parallel}$ and perpendicular $T_{i\perp}$ ion temperature components significantly increase inside the FTEs, $T_{i\parallel}$= +150 eV and $T_{i\perp}$= +100 eV. Panel c represents the acceleration terms, which are boxcar averaged in 2-s intervals. The betatron process, $\dot{U}_{i,2}$ (green), is the dominant acceleration mechanism in this particular event. The contribution by the first order Fermi acceleration process (red) is small, $\dot{U}_{i,3} < 0.3$ nW/m^3, and the acceleration due to parallel electric fields (blue), $\dot{U}_{i,1}$, is shown in Panel c, to be negligible inside and in the environments surrounding the two FTEs (e.g., Dahlin et al., 2016). The latter may suggest the absence of reconnection-driven dynamics, that is, parallel electric fields, at the outer layers of the two FTEs. The scalar sum of the three acceleration mechanisms $\dot{U}_{tot}$ closely matches that of the betatron process. In particular, outside FTEs, $\dot{U}_{i,2}$ is negative suggesting that ions (E × B) drift toward a region of weakening magnetic field, that is, away from the FTE. Inside the FTE, the magnitude of betatron cooling reduces and becomes positive once crossing the FTE's central axis. The Fermi acceleration is negative on the trailing edge of FTE 1, suggesting that the stretched outer magnetic layers at the trailing end of FTE 1 are likely shortening, that is, reduced curvature. Finally, the acceleration signatures, especially the betatron process, have similar profiles across FTE 1 and FTE 2. However, the betatron process is larger in magnitude inside and across the smaller FTE.

Panels d–h show the ion energy spectra binned based on their pitch angle distribution (PAD) with respect to the ambient magnetic field direction. Ion bulk velocity is subtracted from the energy spectra. Each PAD bin is 20° in width. At the leading edge of FTE 1, increased low-energy (E_{ion} [keV] < 0.2) ion differential energy fluxes are observed at PAD <20° and 80 < PAD <100°. While plasma density drops inside FTE 1, the ion differential energy fluxes with 120 < PAD <140° and 160 < PAD <180° increase. At 02:21:00 UT, at the trailing edge of FTE 1, the parallel ion population completely vanishes and the ion distribution becomes predominantly antiparallel, PAD >120°. At this point, the spacecraft enter a higher-energy (0.2 < E_{ion} [keV] < 2.0) magnetosheath ion population with PAD >120°. Once encountering FTE 2, the energy of the antiparallel ions is significantly reduced, and new parallel and perpendicular ion peaks appear, PAD <100°. After crossing FTE 2, the ion population returns to the higher energy (0.2 < E_{ion} [keV] < 2.0) magnetosheath ion population with PAD >120°.

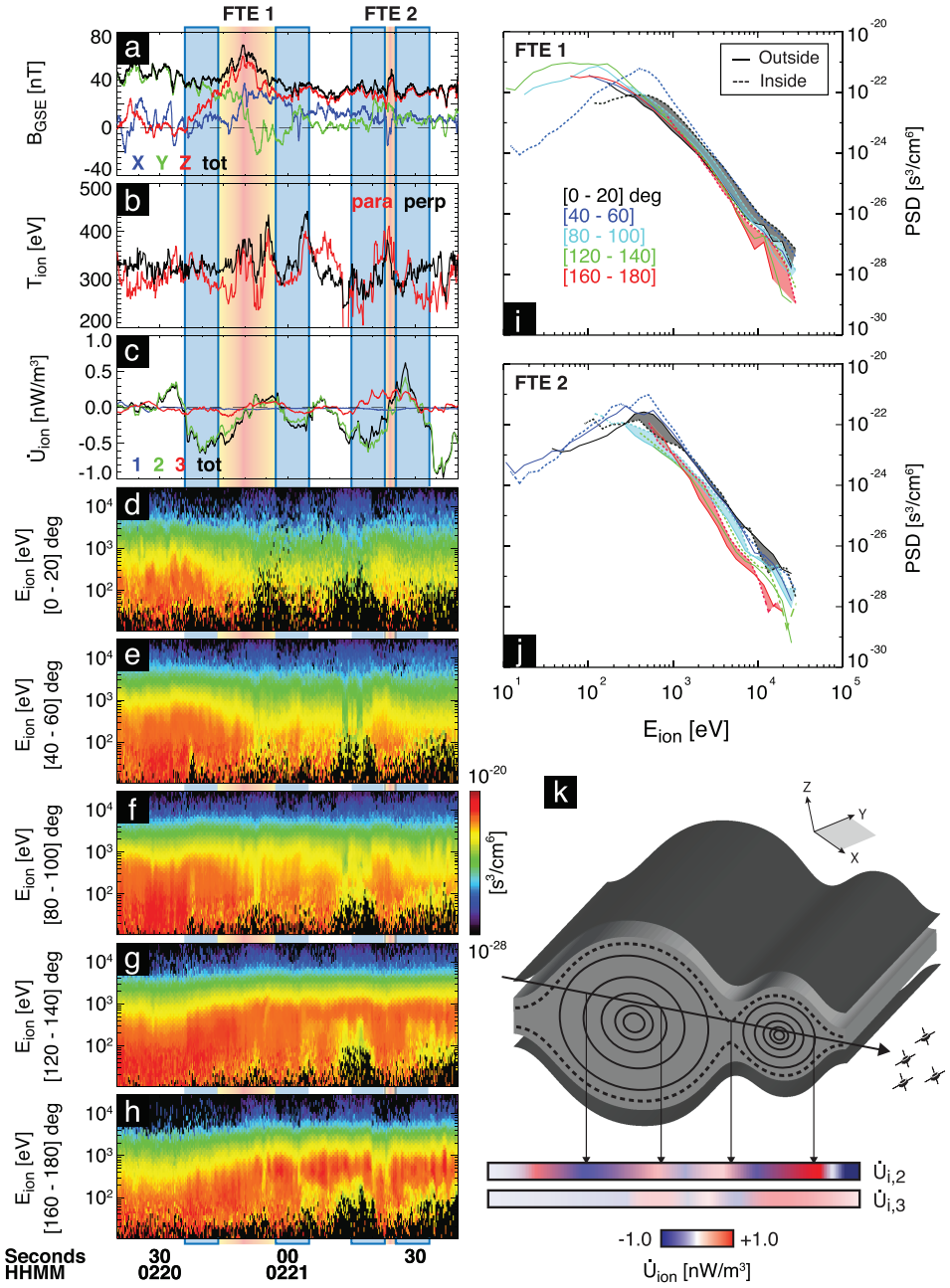

Figure 1. Panels include (a) magnetic field magnitude and components in the *geocentric solar ecliptic system* coordinates, (b) ion parallel (red) and perpendicular (black) temperature components, (c) boxcar-averaged (2 s) ion acceleration mechanisms, $\dot{U}$, due to parallel electric fields (Term 1: blue), betatron acceleration (Term 2: green), and Fermi acceleration (Term 3: red) as well as the scalar sum of the three terms shown in black. Ion energy spectra (bulk ion velocity subtracted) for pitch angle distributions are the following: (d) 0–20°, (e) 40–60°, (f) 80–100°, (g) 120–140°, and (h) 160–180°. The gradient and solid color shadings correspond to the observations made "inside" and "outside" the FTEs, respectively. Time-averaged ion energy spectra inside (dashed line) and outside (solid line) (i) FTE 1 and (j) FTE 2 at five PADs. The shaded areas represent the shift in ion energy inside and outside each FTE. (k) Cartoon schematic of the relative orientations, spacecraft trajectory, and the observed (see Panel c) magnitudes and directions of ion acceleration due to betatron and Fermi acceleration across FTE 1 and FTE 2.

Panels i–j represent the corresponding phase space density (PSD) cuts inside and outside FTE 1 and FTE 2 as a function of ion energy, respectively. The solid lines in Panel i and j are the PSD cut averages outside FTE 1 (02:20:30–02:20:35 UT) and FTE 2 (02:21:25.5–02:21:29.5 UT), respectively. The dashed lines in Panel i and j

are the PSD cut averages inside FTE 1 (02:20:50–02:20:55 UT) and FTE 2 (02:21:24–02:21:24.5 UT), respectively. The shift in energy from outside to inside the FTEs are shaded for three energy bins (black: 0–20°, cyan: 80–100°, and red: 160–180°). The energy shift is, on average, more significant in the larger FTE, FTE 1, than FTE 2. The shift in the mid-to-high energy, $0.2 < E_{ion}$ [keV] < 10.0, ions is also found to be, on average, positive from the environments surrounding the two FTEs to the inside, suggesting that these ions may have been accelerated inside FTEs. More importantly, the aforementioned two observations indicate that the peak ion acceleration inside the larger FTE is more pronounced than the smaller FTE. This may suggest that the plasma inside the larger FTE has been heated for a longer duration, that is, cumulative effect, than those inside the smaller, less-developed FTE.

Panel k demonstrates a cartoon illustration of the spacecraft trajectory across FTE 1 and 2. The magnitude and the sign of the betatron, $\dot{U}_{i,2}$, and Fermi, $\dot{U}_{i,3}$, processes are shown as color shades (red: positive and blue: negative). As shown in Panel c, our observations indicate that the betatron process is larger inside the two FTEs than the Fermi process, therefore, marked in the illustration with darker shades. The contribution from the parallel electric fields is negligible in this particular event, hence, not included in this cartoon illustration. In addition, as the observations suggest, the rate of energization is larger inside and across the smaller FTE.

3.2. Statistical Study

Fifty-five quasi-force-free FTEs are selected at the subsolar region within 22 min of the magnetic noon during 2 months of MMS passes near the equatorial region, 03 November 2015–28 December 2015. The FTEs are identified based on their helical and flux rope-like structures (e.g., Akhavan-Tafti et al., 2018; Russell & Elphic, 1978). Each FTE is initially modeled as a force-free flux rope (Akhavan-Tafti et al., 2018; Lepping et al., 1990) in order to determine the FTE's diameter and the relative distance from its central axis at the closest approach, that is, IP. These information and the high temporal and spatial-resolution MMS fields and plasma measurements enabled us to determine the contributions of the plasma acceleration mechanisms inside and outside FTEs. Here, the term "outside" refers to the FTEs' outer perimeters in the draping field region surrounding each FTE within 10 local ion inertial lengths, d_i (Akhavan-Tafti et al., 2019; Farrugia et al., 1988). Outside FTEs include field lines in the magnetosheath, which, in many cases, are in the near reconnection exhaust regions of X-lines that generated the FTEs (e.g., Lee & Fu, 1985) or contributed to their growth (e.g., Akhavan-Tafti et al., 2019). As shown by Akhavan-Tafti et al. (2019), the electrons and ions remained frozen-in inside the 55 FTEs further validating the guiding center limit.

Figure 2 compares averaged cross-sectional profiles of the energization mechanisms, including parallel electric fields and betatron and first-order Fermi processes, inside and outside FTEs. The observations are further divided between two regions: 1) leading (front) half of the FTE and 2) trailing (rear) half of the FTE. To achieve this, the FTE's convection direction is determined in the spacecraft's frame of reference (Korotova et al., 2009 January). For instance, the spacecraft encounters the leading edge of the FTE, if $\hat{v}_{FTE}\cdot\hat{n}_{S/C} < 0$, where $\hat{v}_{FTE}$ and $\hat{n}_{S/C}$ represent FTE displacement and spacecraft trajectory unit vectors, respectively. IP $= 0$ indicates the central region of the FTE, and IP $= \pm 1$ denotes the FTE front and rear "edges," beyond which the magnetic field connectivity changes, and magnetic fields are no longer bound to the structure (Rijnbeek et al., 1987; Farrugia et al., 1988, 2016). In order to take into account environmental variability between different orbits, all energization terms, $\dot{U}_{i,x}$, are normalized by an analytical weight (Appendix A in Akhavan-Tafti et al., 2019), defined as the ratio of the magnitudes of the universal average of $\dot{U}_{i,x}$, and determined across 55 independent FTE events and inside each individual event.

The acceleration mechanisms observed inside FTEs and$|\dot{U}_x|$ [nW/m^3] < 30.0 (more than 90% of all observations are within $|\dot{U}_x|$[nW/m^3] < 30.0, as shown in Supporting information Figure S1) are binned independently (bin width [BW]: IP $= 0.1$) and averaged across all 55 FTEs. Observations outside the 55 FTEs are bin averaged (BW $= 1\ d_i$; where $d_i = c/\omega_{pi} = 2.28 \times 10^7\ (N_i)^{-1/2}$ cm is the average local ion inertial length and is a function of average ion density, N_i, outside each FTE). The error bars indicate the normalized variations of parameters inside individual bins and are known as the standard error, $\sigma_{mean} \equiv {}^{\sigma}\!\left/\!{}_{\sqrt{n}}\right.$; where σ and n are the standard deviation and the number of data points in each bin, respectively.

Plasma energization inside and at the outer layers of FTEs is asymmetric. Panels a and b show that the acceleration (or deceleration) of ions and electrons is most significant inside FTEs at the leading edge. Ions inside

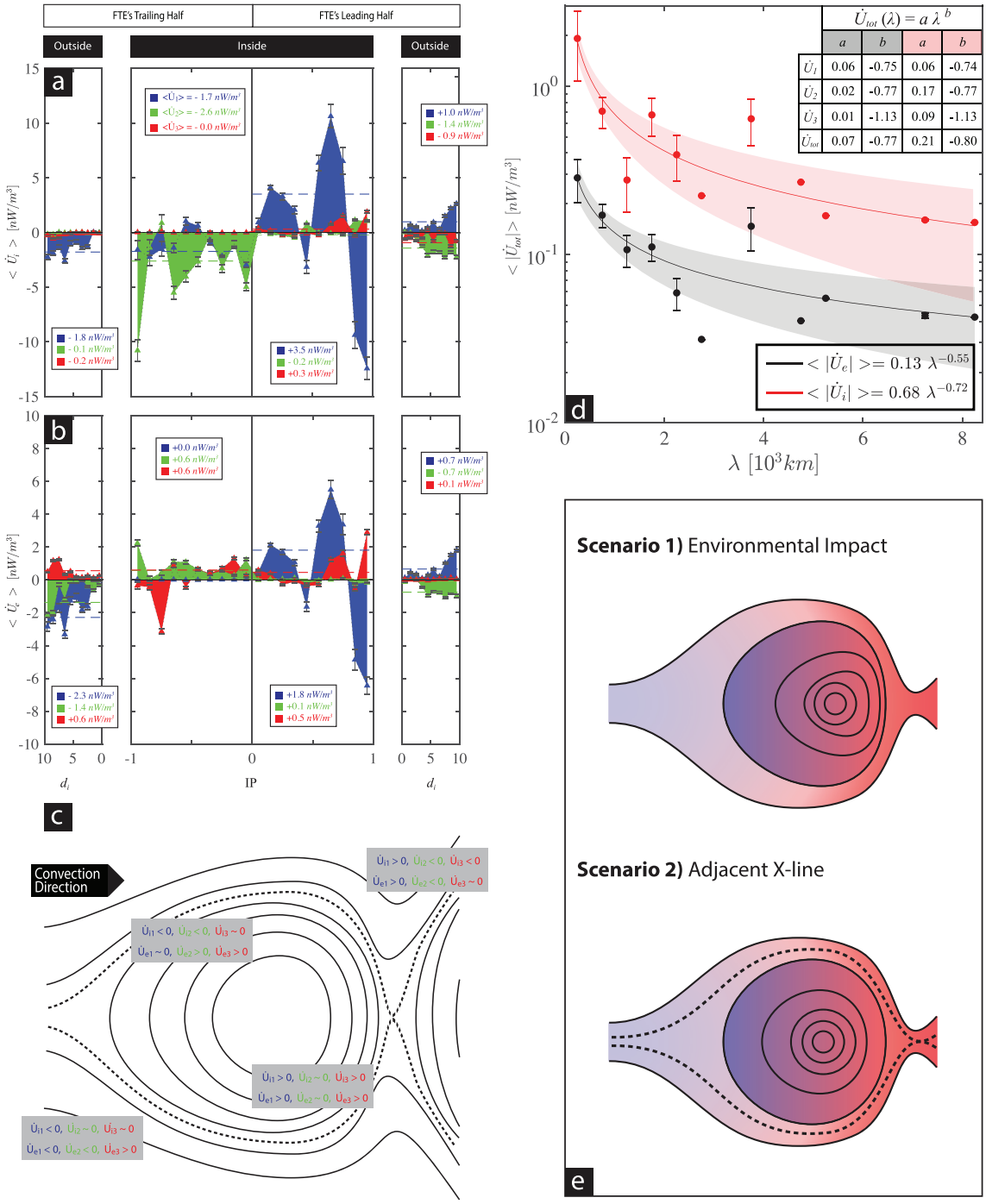

$\dot{U}_{tot}(\lambda) = a\,\lambda^{b}$	a	b	a	b
$\dot{U}_1$	0.06	-0.75	0.06	-0.74
$\dot{U}_2$	0.02	-0.77	0.17	-0.77
$\dot{U}_3$	0.01	-1.13	0.09	-1.13
$\dot{U}_{tot}$	0.07	-0.77	0.21	-0.80

Figure 2. Cross sectional profiles of plasma acceleration mechanisms, including parallel electric field ($\dot{U}_1$: blue), betatron acceleration ($\dot{U}_2$: green), and Fermi acceleration ($\dot{U}_3$: red), inside and outside the 55 FTEs for (a) ions and (b) electrons. All data points inside the 55 FTEs are grouped and averaged inside impact parameter bins of bin width (BW: IP = 0.1). All data points outside the 55 FTEs are grouped and averaged inside bins of BW = 1 d_i. Observations are further divided between the leading and trailing halves. The error bar denotes the standard error inside each individual bin. The dashed line represents the universal average of each parameter across 55 FTEs. (c) Cartoon illustration of a convecting flux rope interacting with the surrounding environment, based on the observations in Panels *a* and *b*. (d) Ion (red) and electron (black) total acceleration magnitudes as a function of FTE diameter across the 55 FTEs. The circles indicate the bin-averaged (BW = 500 km) values of total acceleration. The table represents the dependence of bin-averaged acceleration mechanisms as a function of FTE diameter for both electrons (gray) and ions (red), and (e) cartoon illustrations of two potential scenarios to explain the observed reversal in plasma acceleration near the FTE's central axis. The shading suggests the magnitude and the direction of plasma acceleration wherein red and blue indicate positive and negative values, respectively. The dashed lines represent a reconnection separatrix (and X-line).

the leading part of the FTEs are, on average, net heated, $\dot{U}_{i,x} > 0$, and parallel ($\dot{U}_{i,1} = +3.5$ nW/m^3 and $\dot{U}_{i,3} = +0.3$ nW/m^3) to B. The acceleration magnitude inside the leading part of the FTEs is nearly three times larger than those observed outside, at the leading part of the FTE. Ions and electrons are shown to decelerate perpendicular to the ambient magnetosheath B at the leading and trailing edges of FTEs.

Inside FTEs, ions are net heated parallel to B and net cooled perpendicular to B, whereas electrons experience net parallel and perpendicular heating. Parallel electric fields become the dominant energization mechanism at the leading part of the FTE, accelerating both ions and electrons parallel to B. The acceleration enhances (and fluctuates) farther away from the FTE's core region, IP = 0. Ions are, on average, cooled at the trailing edge of the FTE ($\dot{U}_{i,1} = -1.7$ nW/m^3 and $\dot{U}_{i,2} = -2.6$ nW/m^3). Unlike ions, electrons are, on average, accelerated parallel and perpendicular to B in the trailing half, $\dot{U}_{e,3} = +0.6$ nW/m^3 and $\dot{U}_{e,2} = +0.6$ nW/m^3. The Fermi process is found to steadily accelerate electrons inside FTEs.

Outside FTEs, parallel electric fields remain the most significant of the three energization mechanisms. Parallel electric fields accelerate ions and electrons parallel to B at the leading edge of subsolar FTEs, while they contribute to parallel cooling of the plasma at the trailing edge of the FTE. Outside FTEs at the trailing edge, both ions and electrons are cooled perpendicular to B indicating a region of weakening magnetic field intensity. Similarly, the Fermi process is found to cool both ions and electrons outside the FTEs, suggesting relaxing field lines, that is, reduced curvature. It is also found that the three energization mechanisms enhance in magnitude farther away from the FTE front and rear edges.

Panel c provides a cartoon summary of the observations. As the cartoon illustration indicates, one possible explanation is that FTEs convecting away from the subsolar region may reconnect with the surrounding environment (e.g., Akhavan-Tafti et al., 2019; Øieroset et al., 2019; Zhou et al., 2017), therefore, resulting in the formation of strong parallel electric fields, which can accelerate plasmas (Egedal et al., 2012). The trailing magnetic field lines, on the other hand, continue to relax resulting in cooling ions and reduced electron heating.

We further examine how the rate at which total acceleration, defined as the magnitude of the sum of the three acceleration mechanisms, varies as a function of FTE diameter. Figure 2d shows the change in average total acceleration magnitude as a function of FTE diameter. Here, total acceleration magnitudes are averaged inside individual FTEs and plotted with respect to the FTE diameter. The solid curves represent power law fits to the data with shaded areas demonstrating the 95% confidence interval. The dependence of the total acceleration magnitude as a function of the FTE diameter, λ, is measured on average as $\lambda^{-0.55}$ for electrons and $\lambda^{-0.72}$ for ions. These suggest, in agreement with Figure 1, that acceleration is most significant inside smaller, and likely younger, FTEs. The observations also show that as FTEs grow larger they become more force free (e.g., Akhavan-Tafti et al., 2018; Taylor, 1986) resulting in reduced plasma acceleration. Another likely contributing factor to the observed decline in average heating with FTE diameter may be the reduced gradient scale length (i.e., $\nabla \propto 1/\lambda$).

Total acceleration is reduced with increasing FTE diameter; however, FTE growth continuously accelerates plasmas inside FTEs resulting in higher energy budget than ions and electrons observed inside smaller FTEs. The table on the right-hand corner of Figure 2d further summarizes the coefficients a and b for power law fits for individual electron (gray) and ion (red) acceleration terms as a function of the FTE diameter, $\dot{U} = a\,\lambda^{\,b}$. The values are bin averaged across all 55 FTEs. In particular, plasma heating by parallel electric fields decreases slowly compared to the betatron and Fermi processes. Fermi acceleration is found to drop fastest, $b = -1.13$, with increasing FTE diameter.

4. Discussion and Conclusions

In this letter, we have investigated the contributions of parallel electric fields, betatron, and first-order Fermi processes to plasma acceleration and heating inside FTEs and in the surrounding environments.

First, the MMS plasma and fields measurements are investigated inside a system of two neighboring FTEs with different scale sizes. It is also observed that the betatron process reverses near the FTE's central axis suggesting that ions are decelerated on one side of the FTE, while accelerated on the other side of the FTE, therefore, conserving total energy. As illustrated in Figure 2e, two scenarios may explain this observation:

1. The interaction of FTE-type flux ropes with the surrounding magnetosheath environment (e.g., Fu et al., 2011; Slavin et al., 2003; Zhu et al., 2019) and/or
2. Reconnection-driven interaction with the surrounding environment (e.g., Lapenta et al., 2016), including FTE coalescence (e.g., Wang et al., 2016a; Zhou et al., 2017) and the associated parallel electric fields (e.g., Ergun et al., 2017; Schindler et al., 1988).

In both scenarios, the field lines at the impacted edge of the FTE will be compressed, while the field lines in the opposite edge expand adiabatically (Akhavan-Tafti et al., 2019). Therefore, in order to conserve the first adiabatic invariant $\boldsymbol{\mu}$, the plasmas in the region of compressing field lines, that is, enhanced ∇B (e.g., Øieroset et al., 2019), will gain energy, while the plasma population in the region of expanding field lines, that is, weakening B and ∇B, will have reduced total energy. One possible consequence of this local betatron reversal is the energy (e.g., Matsui et al., 2019) and/or distribution bifurcation (e.g., Artemyev et al., 2014; Zhu et al., 2019) of the differential energy flux of the seed plasma population, wherein part of the seed plasma population is accelerated while others decelerate.

Next, we determine the average contributions of the acceleration processes inside an ensemble of 55 subsolar, quasi-force-free FTEs including the region at their outer perimeters. This region just outside of the FTEs in the magnetosheath is important because, in many cases, it is in the near-reconnection exhaust of adjacent X-line.

Our results show that plasma energization inside and at the outer layers of FTEs is found to be asymmetric. It is further shown that

1. Ions and electrons are, on average, net heated, $\dot{U} > 0$, inside and just outside FTEs. We find that, on average, parallel electric fields are the dominant heating mechanism (70–90% of $\dot{U}_{tot}$) for both ions and electrons, at the leading half of FTEs, in agreement with the kinetic simulation runs by Egedal et al. (2012) and Zhou et al. (2018). At the leading part of the structure, ions and electrons gain further parallel energy via the Fermi process.
2. As listed in the table in Figure 2d, electron heating due to Fermi acceleration is negligible. In contrast, ion heating due to the Fermi process is significant at small FTE scales, though it decreases sharply with increasing FTE diameter. The betatron heating of ions is dominant at small FTE scales. These results and the observed dominant plasma heating by parallel electric fields may indicate the occurrence of secondary reconnection, including FTE coalescence, inside and/or between neighboring FTEs (e.g., Fermo et al., 2011; Wang et al., 2016; Zhou et al., 2017).
3. Inside FTEs, at the leading edge of FTEs, ions and electrons are preferentially accelerated parallel to B (e.g., Shay et al., 2014), farther away from the FTE's central axis, where|B|is reduced. Plasma energization drops by ~75% across the FTE's leading boundary. At the trailing part of FTEs, ions are cooled mainly by the betatron process, and the electron net heating is reduced.
4. Outside FTEs, at the leading edge of FTEs, ions and electrons are accelerated parallel to B by parallel electric fields. Ions are shown to gain, on average, 30% more energy than electrons from parallel electric fields (Haggerty et al., 2015; Pritchett, 2008). At the trailing edge of the FTEs, both ions and electrons are cooled perpendicular to B, indicating a region of relaxing field topology.
5. MMS observations suggest that acceleration mechanisms are enhanced farther away from the FTEs' outer edge. This suggests the following:

    a Farther away from the FTE edge, most likely nearer to the reconnection X-line(s) (e.g., Dahlin et al., 2015; Fu, Peng, et al., 2019), parallel electric fields and magnetic field gradients are most effective in plasma acceleration (see Figure 8 in Zhou et al., 2018), and/or
    b Force-free FTEs may slow down the rate at which plasmas are accelerated in the reconnection exhaust (e.g., Taylor, 1974). As FTEs grow, they seek to reach a lower energy state by rearranging magnetic field lines. At lower magnetic energy state, the trapped plasma population will experience small acceleration compared to the plasmas at the outer boundaries of FTEs near the reconnection exhaust.

6. Statistical analysis of the MMS observations show that the magnitude of the total ion acceleration inside FTEs is proportional to $\lambda^{-0.7}$. However, energetic ions are more often observed inside FTEs of larger diameter. These results suggest that the plasmas inside smaller FTEs are continuously accelerated while the

FTEs grow. Even though the rate at which plasmas are accelerated slows down inside larger FTEs, the total plasma energy budget continues to increase with time, resulting in increased differential flux of energetic ions (e.g., $0.2 < E_{ion}$ [keV] < 10.0) inside FTEs. Similar long-lasting, evolutionary processes may also contribute to the generation of energetic plasmas observed in other plasma environments (e.g., Angelopoulos et al., 2008; Dewey et al., 2017; Fu, Peng, et al., 2019; Ji et al., 1998; Lin et al., 2003; Milan et al., 2000; Øieroset et al., 2002).

The present study focuses on the contributions of parallel electric fields, betatron, and first-order Fermi processes to plasma acceleration and heating inside FTEs and in the surrounding environments. Future studies will further include other key terms such as polarization drift associated with ion acceleration across reconnecting fields with a shear angle (e.g., Eastwood et al., 2018; Kleva et al., 1995; Pritchett & Coroniti, 2004) and ion inertial drift (e.g., Drake et al., 2009; Haggerty et al., 2015; Phan et al., 2014). Global simulations are also essential in understanding the FTE evolution and its role in magnetosheath heating (e.g., Chen et al., 2017; Jarvinen et al., 2018).

Acknowledgments
Research at the University of Michigan was funded by NASA MMS GI grant 80NSSC18K1363, NASA grant 80NSSC18K0999, and the Southwest Research Institute's MMS NASA contract NNG04EB99C. The MMS data can be publicly accessed from the MMS Science Data Center website (https://lasp.colorado.edu/mms/sdc/public/).

References

Akhavan-Tafti, M., Slavin, J. A., Eastwood, J. P., Cassak, P. A., & Gershman, D. J. (2019). MMS multi-point analysis of FTE evolution: Physical characteristics and dynamics. *Journal of Geophysical Research: Space Physics*, *124*, 5376–5395. https://doi.org/10.1029/2018JA026311

Akhavan-Tafti, M., Slavin, J. A., Le, G., Eastwood, J. P., Strangeway, R. J., Russell, C. T., et al. (2018). MMS examination of FTEs at the Earth's subsolar magnetopause. *Journal of Geophysical Research: Space Physics*, *123*, 1224–1241. https://doi.org/10.1002/2017JA024681

Angelopoulos, V., McFadden, J. P., Larson, D., Carlson, C. W., Mende, S. B., Frey, H., et al. (2008). Tail reconnection triggering substorm onset. *Science*, *321*(5891), 931–935. https://doi.org/10.1126/science.1160495

Artemyev, A. V., Walsh, A. P., Petrukovich, A. A., Baumjohann, W., Nakamura, R., & Fazakerley, A. N. (2014). Electron pitch angle/energy distribution in the magnetotail. *Journal of Geophysical Research: Space Physics*, *119*, 7214–7227. https://doi.org/10.1002/2014JA020350

Aschwanden, M. J. (2002). Particle acceleration and kinematics in solar flares. In *Particle Acceleration and Kinematics in Solar Flares* (pp. 1–227). Dordrecht: Springer.

Baker, D. N., & Stone, E. C. (1977). Observations of energetic electrons (E 200 keV) in the Earth's magnetotail: Plasma sheet and fireball observations. *Journal of Geophysical Research*, *82*(10), 1532–1546.

Benz, A. O. (2017). Flare observations. *Living Reviews in Solar Physics*, *14*(1), 2.

Bessho, N., & Bhattacharjee, A. (2012). Fast magnetic reconnection and particle acceleration in relativistic low-density electron-positron plasmas without guide field. *The Astrophysical Journal*, *750*(2), 129. https://doi.org/10.1088/0004-637X/750/2/129

Büchner, J., Kilian, P., Muñoz, P. A., Spanier, F., Widmer, F., Zhou, X., & Jain, N. (2018). Kinetic simulations of electron acceleration at mercury. In *Magnetic Fields in the Solar System* (pp. 201–240). Cham: Springer.

Burch, J. L., Moore, T. E., Torbert, R. B., & Giles, B. L. (2016). Magnetospheric multiscale overview and science objectives. *Space Science Reviews*, *199*(1–4), 5–21.

Cerutti, B., Werner, G. R., Uzdensky, D. A., & Begelman, M. C. (2012). Beaming and rapid variability of high-energy radiation from relativistic pair plasma reconnection. *The Astrophysical Journal*, *754*(2), L33. https://doi.org/10.1088/2041-8205/754/2/L33

Chen, L.-J., Bhattacharjee, A., Puhl-Quinn, P. A., Yang, H., Bessho, N., Imada, S., et al. (2008). Observation of energetic electrons within magnetic islands. *Nature Physics*, *4*(1), 19–23. https://doi.org/10.1038/nphys777

Chen, Y., Tóth, G., Cassak, P., Jia, X., Gombosi, T. I., Slavin, J. A., et al. (2017). Global three-dimensional simulation of Earth's dayside reconnection using a two-way coupled magnetohydrodynamics with embedded particle-in-cell model: Initial results. *Journal of Geophysical Research: Space Physics*, *122*, 10,318–10,335. https://doi.org/10.1002/2017JA024186

Dahlin, J. T., Drake, J. F., & Swisdak, M. (2014). The mechanisms of electron heating and acceleration during magnetic reconnection. *Physics of Plasmas*, *21*(9), 92304. https://doi.org/10.1063/1.4894484

Dahlin, J. T., Drake, J. F., & Swisdak, M. (2015). Electron acceleration in three-dimensional magnetic reconnection with a guide field. *Physics of Plasmas*, *22*(10), 100704.

Dahlin, J. T., Drake, J. F., & Swisdak, M. (2016). Parallel electric fields are inefficient drivers of energetic electrons in magnetic reconnection. *Physics of Plasmas*, *23*(12), 120704.

Dahlin, J. T., Drake, J. F., & Swisdak, M. (2017). The role of three-dimensional transport in driving enhanced electron acceleration during magnetic reconnection. *Physics of Plasmas*, *24*(9), 92110.

Dewey, R. M., Slavin, J. A., Raines, J. M., Baker, D. N., & Lawrence, D. J. (2017). Energetic electron acceleration and injection during dipolarization events in mercury's magnetotail. *Journal of Geophysical Research: Space Physics*, *122*, 12,170–12,188. https://doi.org/10.1002/2017JA024617

Drake, J. F., Arnold, H., Swisdak, M., & Dahlin, J. T. (2019). A computational model for exploring particle acceleration during reconnection in macroscale systems. *Physics of Plasmas*, *26*(1), 12901.

Drake, J. F., Opher, M., Swisdak, M., & Chamoun, J. N. (2010). A magnetic reconnection mechanism for the generation of anomalous cosmic rays. *The Astrophysical Journal*, *709*(2), 963–974. https://doi.org/10.1088/0004-637X/709/2/963

Drake, J. F., Swisdak, M., Che, H., & Shay, M. A. (2006). Electron acceleration from contracting magnetic islands during reconnection. *Nature*, *443*(7111), 553–556. https://doi.org/10.1038/nature05116

Drake, J. F., Swisdak, M., Phan, T. D., Cassak, P. A., Shay, M. A., Lepri, S. T., et al. (2009). Ion heating resulting from pickup in magnetic reconnection exhausts. *Journal of Geophysical Research*, *114*, A05111. https://doi.org/10.1029/2008JA013701

Eastwood, J. P., Mistry, R., Phan, T. D., Schwartz, S. J., Ergun, R. E., Drake, J. F., et al. (2018). Guide field reconnection: Exhaust structure and heating. *Geophysical Research Letters*, *45*, 4569–4577. https://doi.org/10.1029/2018GL077670

Egedal, J., Daughton, W., & Le, A. (2012). Large-scale electron acceleration by parallel electric fields during magnetic reconnection. *Nature Physics*, *8*(4), 321.

Ergun, R. E., Chen, L.-J., Wilder, F. D., Ahmadi, N., Eriksson, S., Usanova, M. E., et al. (2017). Drift waves, intense parallel electric fields, and turbulence associated with asymmetric magnetic reconnection at the magnetopause. *Geophysical Research Letters*, *44*, 2978–2986. https://doi.org/10.1002/2016GL072493

Ergun, R. E., Tucker, S., Westfall, J., Goodrich, K. A., Malaspina, D. M., Summers, D., et al. (2016). The axial double probe and fields signal processing for the MMS mission. *Space Science Reviews*, *199*(1–4), 167–188. https://doi.org/10.1007/s11214-014-0115-x

Farrugia, C. J., Lavraud, B., Torbert, R. B., Argall, M., Kacem, I., Yu, W., et al. (2016). MMS observations and non-force free modeling of a flux transfer event immersed in a super-Alfvénic flow. *Geophysical Research Letters*, *43*, 6070–6077. https://doi.org/10.1002/2016GL068758

Farrugia, C. J., Rijnbeek, R. P., Saunders, M. A., Southwood, D. J., Rodgers, D. J., Smith, M. F., et al. (1988). A multi-instrument study of flux transfer event structure. *Journal of Geophysical Research*, *93*(A12), 14465. https://doi.org/10.1029/JA093iA12p14465

Fermo, R. L., Drake, J. F., Swisdak, M., & Hwang, K. J. (2011). Comparison of a statistical model for magnetic islands in large current layers with Hall MHD simulations and cluster FTE observations. *Journal of Geophysical Research*, *116*, A09226. https://doi.org/10.1029/2010JA016271

Fu, H. S., Peng, F. Z., Liu, C. M., Burch, J. L., Gershman, D. G., & Le Contel, O. (2019). Evidence of electron acceleration at a reconnecting magnetopause. *Geophysical Research Letters*, *46*, 5645–5652. https://doi.org/10.1029/2019GL083032

Fu, H. S., Xu, Y., Vaivads, A., & Khotyaintsev, Y. V. (2019). Super-efficient electron acceleration by an isolated magnetic reconnection. *The Astrophysical Journal Letters*, *870*(2), L22.

Fu, H. S., Khotyaintsev, Y. V., André, M., & Vaivads, A. (2011). Fermi and betatron acceleration of suprathermal electrons behind dipolarization fronts. *Geophysical Research Letters*, *38*, L16104. https://doi.org/10.1029/2011GL048528

Guo, F., Liu, Y.-H., Daughton, W., & Li, H. (2015). Particle acceleration and plasma dynamics during magnetic reconnection in the magnetically-dominated regime. *The Astrophysical Journal*, *806*(2). Retrieved from. https://arxiv.org/abs/1504.02193

Haggerty, C. C., Shay, M. A., Drake, J. F., Phan, T. D., & McHugh, C. T. (2015). The competition of electron and ion heating during magnetic reconnection. *Geophysical Research Letters*, *42*, 9657–9665. https://doi.org/10.1002/2015GL065961

Harvey, C. C. (1998). Spatial gradients and the volumetric tensor. In *Analysis Methods for Multi-Spacecraft Data / Götz Paschmann and Patrick Daly*, *ISSI Scientific Reports Series, ESA/ISSI* (Vol. 1. ISBN 1608-280X, 1998, pp. 307–322). Retrieved from. http://www.issibern.ch/forads/sr-001-12.pdf

Hoilijoki, S., Ganse, U., Sibeck, D. G., Cassak, P. A., Turc, L., Battarbee, M., et al. (2019). Properties of magnetic reconnection and FTEs on the dayside magnetopause with and without positive IMF B component during southward IMF. *Journal of Geophysical Research: Space Physics*, *124*, 4037–4048. https://doi.org/10.1029/2019JA026821

Hoshino, M., Mukai, T., Terasawa, T., & Shinohara, I. (2001). Suprathermal electron acceleration in magnetic reconnection. *Journal of Geophysical Research*, *106*(A11), 25979–25997. https://doi.org/10.1029/2001JA900052

Huang, S. Y., Vaivads, A., Khotyaintsev, Y. V., Zhou, M., Fu, H. S., Retinò, A., et al. (2012). Electron acceleration in the reconnection diffusion region: Cluster observations. *Geophysical Research Letters*, *39*, L11103. https://doi.org/10.1029/2012GL051946

Jaroschek, C. H., Lesch, H., & Treumann, R. A. (2004). Self-consistent diffusive lifetimes of Weibel magnetic fields in gamma-ray bursts. *The Astrophysical Journal*, *616*(2), 1065–1071. https://doi.org/10.1086/424923

Jarvinen, R., Vainio, R., Palmroth, M., Juusola, L., Hoilijoki, S., Pfau-Kempf, Y., et al. (2018). Ion acceleration by flux transfer events in the terrestrial magnetosheath. *Geophysical Research Letters*, *45*, 1723–1731. https://doi.org/10.1002/2017GL076192

Ji, H., Yamada, M., Hsu, S., & Kulsrud, R. (1998). Experimental test of the Sweet–Parker model of magnetic reconnection. *Physical Review Letters*, *80*(15), 3256.

Kagan, D., Nakar, E., & Piran, T. (2017). Physics of the saturation of particle acceleration in relativistic magnetic reconnection. *ArXiv Preprint ArXiv:1711.08701*.

Kleva, R. G., Drake, J. F., & Waelbroeck, F. L. (1995). Fast reconnection in high temperature plasmas. *Physics of Plasmas*, *2*(1), 23–34.

Korotova, G. I., Sibeck, D. G., & Rosenberg, T. (2009 January). Geotail observations of FTE velocities. In *Annales Geophysicae* (Vol. 27, pp. 83–92). Copernicus GmbH.

Kowal, G., Pino, D., de Gouveia Dal Pino, E. M., & Lazarian, A. (2011). Magnetohydrodynamic simulations of reconnection and particle acceleration: three-dimensional effects. *The Astrophysical Journal*, *735*(2), 102.

Krimigis, S. M., & Sarris, E. T. (1979). Energetic particle bursts in the Earth's magnetotail. In *Dynamics of the Magnetosphere* (pp. 599–630). Dordrecht: Springer.

Krucker, S., Battaglia, M., Cargill, P. J., Fletcher, L., Hudson, H. S., MacKinnon, A. L., et al. (2008). Hard X-ray emission from the solar corona. *The Astronomy and Astrophysics Review*, *16*(3–4), 155–208. https://doi.org/10.1007/s00159-008-0014-9

Lapenta, G., Goldman, M., Newman, D., & Markidis, S. (2016). Where should MMS look for electron diffusion regions? *Journal of Physics: Conference Series*, *719*, 12011.

Lee, L. C., & Fu, Z. F. (1985). A theory of magnetic flux transfer at the Earth's magnetopause. *Geophysical Research Letters*, *12*(2), 105–108. https://doi.org/10.1029/GL012i002p00105

Lepping, R. P., Jones, J. A., & Burlaga, L. F. (1990). Magnetic field structure of interplanetary magnetic clouds at 1 AU. *Journal of Geophysical Research*, *95*(A8), 11957. https://doi.org/10.1029/JA095iA08p11957

Lin, R. P. C., Krucker, S., Hurford, G. J., Smith, D. M., Hudson, H. S., Holman, G. D., et al. (2003). RHESSI observations of particle acceleration and energy release in an intense solar gamma-ray line flare. *The Astrophysical Journal Letters*, *595*(2), L69–L76. https://doi.org/10.1086/378932

Lindqvist, P.-A. P.-A., Olsson, G., Torbert, R. B., King, B., Granoff, M., Rau, D., et al. (2016). The spin-plane double probe electric field instrument for MMS. *Space Science Reviews*, *199*(1–4), 137–165. https://doi.org/10.1007/s11214-014-0116-9

Lv, L., Pu, Z., & Xie, L. (2016). Multiple magnetic topologies in flux transfer events: THEMIS measurements. *Science China Technological Sciences*, *59*(8), 1283–1293. https://doi.org/10.1007/s11431-016-6071-9

Lyubarsky, Y., & Liverts, M. (2008). Particle acceleration in the driven relativistic reconnection. *The Astrophysical Journal*, *682*(2), 1436–1442. https://doi.org/10.1086/589640

Matsui, H., Farrugia, C. J., Goldstein, J., Torbert, R. B., Argall, M. R., Vaith, H., et al. (2019). Velocity rotation events in the outer magnetosphere near the magnetopause. *Journal of Geophysical Research: Space Physics*, *124*, 4137–4156. https://doi.org/10.1029/2019JA026548

Meng, C.-I. (1971). Energetic electrons in the magnetotail at 60RE. *Journal of Geophysical Research*, *76*(4), 862–872.

Meng, C.-I., & Anderson, K. A. (1971). Energetic electrons in the plasma sheet out to 40 RE. *Journal of Geophysical Research*, *76*(4), 873–882.

Milan, S. E., Lester, M., Cowley, S. W. H., & Brittnacher, M. (2000). Convection and auroral response to a southward turning of the IMF: Polar UVI, CUTLASS, and IMAGE signatures of transient magnetic flux transfer at the magnetopause. *Journal of Geophysical Research*, *105*(A7), 15741–15755. https://doi.org/10.1029/2000JA900022

Miller, J. A., Cargill, P. J., Emslie, A. G., Holman, G. D., Dennis, B. R., LaRosa, T. N., et al. (1997). Critical issues for understanding particle acceleration in impulsive solar flares. *Journal of Geophysical Research*, *102*(A7), 14,631–14,659. https://doi.org/10.1029/97JA00976

Muñoz, P. A., & Buechner, J. (2017). Two-stage electron acceleration by 3D collisionless guide field magnetic reconnection. *ArXiv Preprint ArXiv:1705.01066*.

Murayama, T., & Simpson, J. A. (1968). Electrons within the neutral sheet of the magnetospheric tail. *Journal of Geophysical Research*, *73*(3), 891–905.

Northrop, T. G. (1963). Adiabatic charged-particle motion. *Reviews of Geophysics*, *1*(3), 283. https://doi.org/10.1029/RG001i003p00283

Øieroset, M., Lin, R. P., Phan, T. D., Larson, D. E., & Bale, S. D. (2002). Evidence for electron acceleration up to ∼300 keV in the magnetic reconnection diffusion region of Earth's magnetotail. *Physical Review Letters*, *89*(19), 195001. https://doi.org/10.1103/PhysRevLett.89.195001

Øieroset, M., Phan, T. D., Drake, J. F., Eastwood, J. P., Fuselier, S. A., Strangeway, R. J., et al. (2019). Reconnection with magnetic flux pileup at the interface of converging jets at the magnetopause. *Geophysical Research Letters*, *46*, 1937–1946. https://doi.org/10.1029/2018GL080994

Oka, M., Fujimoto, M., Shinohara, I., & Phan, T. D. (2010). "Island surfing" mechanism of electron acceleration during magnetic reconnection. *Journal of Geophysical Research*, *115*, A08223. https://doi.org/10.1029/2010JA015392

Phan, T. D., Drake, J. F., Shay, M. A., Gosling, J. T., Paschmann, G., Eastwood, J. P., et al. (2014). Ion bulk heating in magnetic reconnection exhausts at Earth's magnetopause: Dependence on the inflow Alfvén speed and magnetic shear angle. *Geophysical Research Letters*, *41*, 7002–7010. https://doi.org/10.1002/2014GL061547

Pollock, C., Moore, T., Jacques, A., Burch, J., Gliese, U., Saito, Y., et al. (2016). Fast plasma investigation for magnetospheric multiscale. *Space Science Reviews*, *199*(1–4), 331–406. https://doi.org/10.1007/s11214-016-0245-4

Pritchett, P. L. (2008). Energetic electron acceleration during multi-island coalescence. *Physics of Plasmas*, *15*(10), 102105. https://doi.org/10.1063/1.2996321

Pritchett, P. L., & Coroniti, F. V. (2004). Three-dimensional collisionless magnetic reconnection in the presence of a guide field. *Journal of Geophysical Research*, *109*, A01220. https://doi.org/10.1029/2003JA009999

Raeder, J. (2006). Flux transfer events: 1. Generation mechanism for strong southward IMF. *Annales Geophysicae*, *24*, 381.

Retinò, A., Nakamura, R., Vaivads, A., Khotyaintsev, Y., Hayakawa, T., Tanaka, K., et al. (2008). Cluster observations of energetic electrons and electromagnetic fields within a reconnecting thin current sheet in the Earth's magnetotail. *Journal of Geophysical Research*, *113*, A12215. https://doi.org/10.1029/2008JA013511

Retzler, J., & Simpson, J. A. (1969). Relativistic electrons confined within the neutral sheet of the geomagnetic tail. *Journal of Geophysical Research*, *74*(9), 2149–2160.

Rijnbeek, R. P., Farrugia, C. J., Southwood, D. J., Dunlop, M. W., Mier-Jedrzejowicz, W. A. C., Chaloner, C. P., et al. (1987). A magnetic boundary signature within flux transfer events. *Planetary and Space Science*, *35*(7), 871–878. https://doi.org/10.1016/0032-0633(87)90065-1

Russell, C. T., & Elphic, R. C. (1978). Initial ISEE magnetometer results: Magnetopause observations. *Space Science Reviews*, *22*(6), 681–715.

Russell, C. T., Anderson, B. J., Baumjohann, W., Bromund, K. R., Dearborn, D., Fischer, D., et al. (2016). The Magnetospheric Multiscale Magnetometers. *Space Science Reviews*, *199*(1–4), 189–256. https://doi.org/10.1007/s11214-014-0057-3

Sarris, E. T., Krimigis, S. M., & Armstrong, T. P. (1976). Observations of magnetospheric bursts of high-energy protons and electrons at~ 35 RE with Imp 7. *Journal of Geophysical Research*, *81*(13), 2341–2355.

Schindler, K., Hesse, M., & Birn, J. (1988). General magnetic reconnection, parallel electric fields, and helicity. *Journal of Geophysical Research*, *93*(A6), 5547–5557.

Shay, M. A., Haggerty, C. C., Phan, T. D., Drake, J. F., Cassak, P. A., Wu, P., et al. (2014). Electron heating during magnetic reconnection: A simulation scaling study. *Physics of Plasmas*, *21*(12), 122902. https://doi.org/10.1063/1.4904203

Slavin, J. A., Lepping, R. P., Gjerloev, J., Fairfield, D. H., Hesse, M., Owen, C. J., et al. (2003). Geotail observations of magnetic flux ropes in the plasma sheet. *Journal of Geophysical Research*, *108*(A1), 1015. https://doi.org/10.1029/2002JA009557

Taylor, J. B. (1974). Relaxation of toroidal plasma and generation of reverse magnetic fields. *Physical Review Letters*, *33*(19), 1139.

Taylor, J. (1986). Relaxation and magnetic reconnection in plasmas. *Reviews of Modern Physics*, *58*(3), 741.

Torbert, R. B., Russell, C. T., Magnes, W., Ergun, R. E., Lindqvist, P.-A., LeContel, O., et al. (2016). The FIELDS instrument suite on MMS: Scientific objectives, measurements, and data products. *Space Science Reviews*, *199*(1–4), 105–135. https://doi.org/10.1007/s11214-014-0109-8

Uzdensky, D. A., Cerutti, B., & Begelman, M. C. (2011). Reconnection-powered linear accelerator and gamma-ray flares in the crab nebula. *The Astrophysical Journal*, *737*(2), L40. https://doi.org/10.1088/2041-8205/737/2/L40

Wang, R., Lu, Q., Nakamura, R., Huang, C., Du, A., Guo, F., et al. (2016). Coalescence of magnetic flux ropes in the ion diffusion region of magnetic reconnection. *Nature Physics*, *12*(3), 263–267. https://doi.org/10.1038/nphys3578

Zenitani, S., & Hoshino, M. (2001). The generation of nonthermal particles in the relativistic magnetic reconnection of pair plasmas. *The Astrophysical Journal*, *562*(1), L63–L66. https://doi.org/10.1086/337972

Zenitani, S., & Hoshino, M. (2007). Particle acceleration and magnetic dissipation in relativistic current sheet of pair plasmas. *The Astrophysical Journal*, *670*(1), 702–726. https://doi.org/10.1086/522226

Zenitani, S., & Hoshino, M. (2008). The role of the guide field in relativistic pair plasma reconnection. *The Astrophysical Journal*, *677*(1), 530–544. https://doi.org/10.1086/528708

Zhao, C., Russell, C. T., Strangeway, R. J., Petrinec, S. M., Paterson, W. R., Zhou, M., et al. (2016). Force balance at the magnetopause determined with MMS: Application to flux transfer events. *Geophysical Research Letters*, *43*, 11,941–11,947. https://doi.org/10.1002/2016GL071568

Zhou, M., Berchem, J., Walker, R. J. J., El-Alaoui, M., Deng, X., Cazzola, E., et al. (2017). Coalescence of macroscopic flux ropes at the subsolar magnetopause: Magnetospheric multiscale observations. *Physical Review Letters*, *119*(5), 055101. https://doi.org/10.1103/PhysRevLett.119.055101

Zhou, M., El-Alaoui, M., Lapenta, G., Berchem, J., Richard, R. L., Schriver, D., & Walker, R. J. (2018). Suprathermal electron acceleration in a reconnecting magnetotail: Large-scale kinetic simulation. *Journal of Geophysical Research: Space Physics*, *123*, 8087–8108. https://doi.org/10.1029/2018JA025502

Zhu, C., Zhang, H., Fu, S., Ni, B., Strangeway, R. J., Giles, B. L., et al. (2019). Trapped and accelerated electrons within a magnetic mirror behind a flux rope on the magnetopause. *Journal of Geophysical Research: Space Physics*, *124*, 3993–4008. https://doi.org/10.1029/2019JA026464